AIChE WILEY InterScience DISCOVER SOMETHING GREAT

PROCESS SYSTEMS ENGINEERING

Discovery of Transport and Reaction Properties in Distributed Systems

Libin Zhang, Kedar Kulkarni, MahadevaBharath R. Somayaji, Michalis Xenos, and Andreas A. Linninger
Laboratory for Product and Process Design, University of Illinois at Chicago, Chicago, IL 60607

DOI 10.1002/aic.11018
Published online December 20, 2006 in Wiley InterScience (www.interscience.wiley.com).

In distributed systems, transport phenomena coupled with chemical or metabolic reactions are functions of space. A computational method is outlined to acquire unknown system properties in distributed systems by problem inversion. *Physical and chemical properties are estimated simultaneously. The finite-volume discretization method formulated in generalized curvilinear coordinates applied to inversion problem of arbitrarily complex geometries. The direct solution approach of the reacting transport problem through inexpensive acquisition of sensitivity information is presented. An inexact trust region method improves the convergence rate of the large-scale* transport and kinetic inversion problem (TKIP). *The case studies demonstrate a novel computational approach for quantifying unknown transport properties, as well as reaction or metabolic constants. Solutions to technological challenges is presented in computational fluid mechanics and biotransport using mathematical programming techniques for inversion of distributed systems.* © 2006 American Institute of Chemical Engineers *AIChE J*, 53: 381–396, 2007
Keywords: problem inversion, generalized curvilinear transformation, finite volume method, inexact trust region method

Introduction

Many chemical processes are characterized by strong coupling between heat, mass- and momentum-transfer. Existing parameter estimation techniques focus mostly on chemical-kinetic mechanisms without spatial dependence or attention to transport phenomena like convection and diffusion. Those techniques rely on perfect mixing, which can often not be achieved in the real processes. Moreover, in many biological systems and safety critical applications, lumped system assumptions are not always justified. Simplified chemical reaction kinetic models without regard to transport phenomena have limited predictive power; thus, their extrapolation to larger reactor dimensions or different configuration can become unreliable.

Parameter estimation in distributed systems involves computationally intensive models with partial-differential equation constraints (PDE). Recently, problem inversion for reaction mechanisms in metallorganic vapor decomposition processes microelectronic applications was studied.[1] Prior research performed data assimilation for air pollution and weather models.[2–5] Inverse problems aim at preventing excessive aerodynamic heating of space vehicles during reentry into the earth's atmosphere.[6] Inversion permits shape optimization in aerodynamic design or reconstructs of tissue optical property maps from photon migration experiments.[7–11] Most of previous inversion problems have not addressed reacting systems with coupled transport in complex distributed domains.

This article proposes the simultaneous estimation of kinetic and transport properties in chemically reactive systems with spatial distribution. Physical experiments in complex geometry will provide the experimental evidence to determine the apparent reaction and transport mechanisms. The procedure to infer unknown reaction and transport properties from distributed experimental data will be termed a *transport and kinetic inversion problem* (TKIP).

Outline. The mathematical formulation for *transport and kinetic inversion* is introduced in the Problem Formulation

Correspondence concerning this article should be addressed to A. A. Linninger at linninge@uic.edu.

section. The finite volume method for the discretization of partial differential equations in complex domains will be discussed in section three. Optimal transport and kinetic properties will be obtained by minimizing the least-squared error sum between the distributed experimental measurements and first-principles mathematical models. Robust and efficient mathematical programming techniques specifically suited for TKIP are introduced in the section mathematical solution approaches for TKIP. The applications and computational results section demonstrates three advanced case studies: identification of unknown metabolic reaction rates of therapeutic drugs in human brain; identification of the nuclear heat generation and transfer in safety-critical plutonium storage vessel; and the dynamics of reaction kinetics and transport mechanics in catalytic pellet reactor. The computational performance of problem inversion section compares the performance of different mathematical programming approaches for inversion problems. It also proposes second-order response surfaces to improve the robustness and convergence rate of the inversion problem. This article closes with significance and conclusions.

Problem Formulation

Problem inversion seeks to quantify chemical kinetic and transport phenomena based on distributed experimental data, such as concentration, flow velocity or temperature measurements obtained at different spatial positions and instances of time. The unknown coefficients in conservation of mass, species and momentum are determined by least-square minimization between data and first-principle mathematical models. The confidence in the models' parameters with respect to given experimental data will be computed simultaneously as an indicator of model quality.

A TKIP as shown in system (1, 2) has three elements: (i) experimental data, (ii) a first-principle mathematical model, and (iii) a problem inversion algorithm. Given *experimental data* are measurements of state variables $\hat{\phi}(x, t)$ at location x, and time t, such as species concentrations, temperatures or flow-velocity measurements. *First principles mathematical models* quantify the distributed states $\phi(x,t,\theta)$, in terms of unknown reaction and transport properties θ. The system of constraints (Eq. 2) represent generically conservation laws for mass ($\phi = 1$), momentum ($\phi = u$), species ($\phi = C$) or energy transfer ($\phi = H$). Their parameter set θ, may include unknown properties related to transport, such as diffusivity, porosity and permeability, as well as reaction-kinetic parameters appearing in source terms S. The *mathematical programming algorithm* determines the optimal parameter set θ by minimizing the weighted least-squared error sum between the data and models.

System 1–2 introduces a mathematical program with partial-differential equation constraints (PDE). Its objective function $\psi(\theta)$, measures the cumulative weighted least-squared error between the model ϕ, and measurements $\hat{\phi}$ in different positions, x_i at time t_i. The covariance matrix F accounts for measurement accuracy of experimental data.

$$\min_{\theta,\phi} \psi(\theta) = (\phi(x,t,\theta) - \hat{\phi}(x,t))^T F^{-1} (\phi(x,t,\theta) - \hat{\phi}(x,t)) \quad (1)$$

s. t.

$$\frac{\partial(\rho\phi)}{\partial t} + \rho\nabla(\vec{u}\phi) = \nabla(\Gamma\nabla\phi) + S(x,\theta,\phi) \quad (2)$$

A direct analytical solution of 1–2 is not possible in general. Two main ideas will help solve this problem numerically: Discretization of the transport equations using the finite-volume approach and efficient and robust mathematical programming algorithms that take advantage of response surfaces to quantify parameter sensitivity.

Mathematical Treatment of the Transport Equations

This section discusses the discretization of the transport equations and introduces curvilinear coordinate transformations to express conservation laws in arbitrarily complex problem domains.

Discretization of transport equations in generalized coordinates

The solution of the nonlinear optimization problem requires the discretization of the PDE constraints in (Eq. 2). We recommend the finite volume approach, because the same discretization scheme applies readily to heat, mass- and momentum-transfer.[12,13] In addition, it ensures integral mass conservation; this property is harder to enforce in finite differences or finite elements. The finite volume method divides the problem domain into a computational mesh composed of a discrete set of balance envelopes. Integration of the conservation laws over each volume renders a set of algebraic-balance equations to replace the continuous PDE constraints. Before deriving finite-volume balances, generalized curvilinear coordinate transformations need to be introduced.

Generalized Coordinates. Chemical and biological processes often occur in domains with complex boundaries for which Cartesian meshes do not apply.[12,14] Generalized curvilinear coordinate transformations permit the accurate solution of transport problems in arbitrarily shaped problem domains. The coordinate transformation converts distorted shapes in physical space into orthogonal balance envelopes so that volume integrals can easily be solved numerically. The metrics of this transformation x_ξ, x_η, y_ξ and y_η can easily be computed locally on each grid cell as shown in Figure 1. The determinant of the inverse Jacobian $|J^{-1}|$ of each volume is given by $|J^{-1}| = x_\xi y_\eta - x_\eta y_\xi$. The metrics of transformation help balance the diffusive and convective-transport properties (ϕ) over an arbitrarily shaped domain of finite volumes. For example, the finite volume balance of a two-dimensional (2-D)-diffusion equation can be expressed in generalized coordinate system (ξ, η) as described in Eq. 3. Transformed equations for relevant transport problems are given in the Appendix A.

$$\int_{dV} \left(\rho\frac{\partial(U\phi)}{\partial\xi} + \rho\frac{\partial(V\phi)}{\partial\eta} - \left[\frac{\partial}{\partial\xi}\left(\Gamma\left[\frac{q_1}{|J^{-1}|}\frac{\partial\phi}{\partial\xi} - \frac{q_2}{|J^{-1}|}\frac{\partial\phi}{\partial\eta} \right] \right) + \frac{\partial}{\partial\eta}\left(\Gamma\left[\frac{q_3}{|J^{-1}|}\frac{\partial\phi}{\partial\eta} - \frac{q_2}{|J^{-1}|}\frac{\partial\phi}{\partial\xi} \right] \right) \right] - |J^{-1}|S \right) \times d\xi d\eta = 0 \quad (3)$$

Finite Volume Method. The coordinate transformation renders rectangular balance envelopes even for irregular shapes in the physical domain. Consequently, the conservation balances

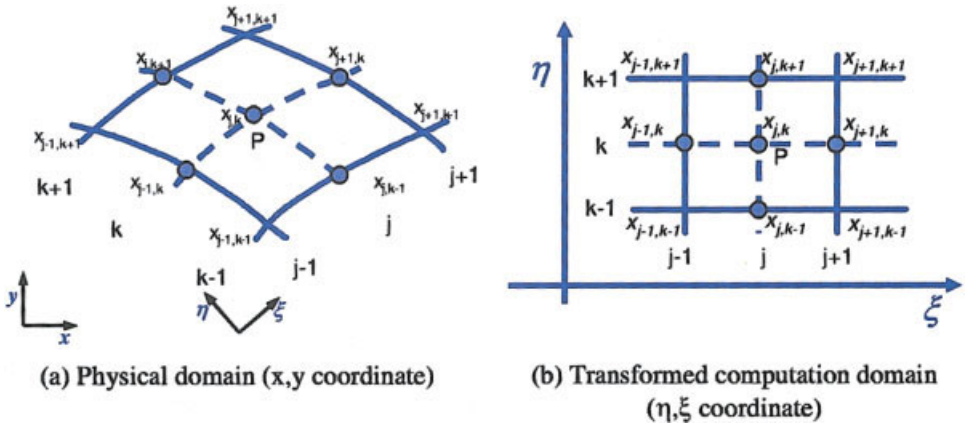

Figure 1. An arbitrary balance envelope in the physical (a), and the generalized coordinate space (b).

[Color figure can be viewed in the online issue, which is available at www.interscience.wiley.com.]

for the transport quantity ϕ, expressed in Eq. 3 can be integrated under proper profile assumptions along the orthogonal ξ- and η- directions. Volume integration over each grid cell yields algebraic expression for the property ϕ, as given in Eq. 4.[15] The system of Eq. 4 expressed in generalized curvilinear coordinates represents the discrete finite volume balances instead of the continuous PDEs in (2). The algebraic system $h(\phi, \theta)$ depends on the state variables ϕ, and the parameters θ, which in turn may include unknown-transport coefficients Γ, and reaction constants k, in source terms S. The mathematical equations for different transport problems are given in Table B1 of Appendix B.

$$h(x, \phi, \theta) = a_p(x, \theta) \cdot \phi_p - \Sigma a_{nb}(x, \theta) \cdot \phi_{nb} - S(x, \phi, \theta) \cdot |j^{-1}| = 0 \quad \forall \; volume \; \theta = \{\Gamma, k\} \tag{4}$$

The discretization of the PDE constraints as well as the boundary conditions renders the TKIP a large-scale nonlinear-optimization problem (NLP). To solve this NLP, we propose a reduced space optimization with the inexact trust region method.

Direct Solution Approach. The classical finite volume methods use the Simple algorithm which elegantly solves the incompressible Navier-Stokes equations by fixed point iteration.[13] In coupled transport and reaction problems, ensuring the convergence of fixed-point methods is problematic. In reacting-flow systems, even extreme under-relaxation does not guarantee convergence. Moreover, existing relaxation methods do not yield gradient and sensitivity information required in large-scale inversion problems. Instead, we advocate the direct solution approach of the transport problem as proposed by Khinast.[16] In addition to increased robustness, direct solution permits the computation of sensitivity information with the help of response surface approximations as discussed next.[17–19]

Sensitivity information response maps and parametric sensitivity

The numerical solution of the large-scale TKIP with gradient-based algorithms, requires expressions for state variable dependence with respect to each parameter $\frac{\partial \phi}{\partial \theta}$, in each iteration. We will show how the sensitivity terms $\frac{\partial \phi}{\partial \theta}$, needed can be obtained by solving a linear algebraic problem. There are two approaches to obtain the sensitivity equations for partial-differential equation constraints. One is to differentiate the original PDEs by the chain rule, and then discretize the sensitivity equations (PDE form) using finite volume approach on the same grid. The other one directly differentiates the discretized state variables with respect to each parameter. Both methods yield the similar results with static computational grids. The second method provides mathematically consistent derivatives for optimization algorithm. In this article, the sensitivity equations are directly obtained from the discretized form of original equations. The analytical derivative of the sensitivity equation is given in Eq. 5, with the help of the chain rule.[20,21] The complete sensitivity information for the TKIP is composed of $M \times N$ sensitivity equations, where M is the total number of unknown state variables of transport equation, and N is the number of optimization parameters.

$$\sum_{i=1}^{M} \frac{\partial h}{\partial \phi_i}\bigg|_{\theta,\phi} \frac{\partial \phi_i}{\partial \theta_j} + \frac{\partial h}{\partial \theta_j}\bigg|_{\theta,\phi} = 0 \quad j = 1, \ldots, N \tag{5}$$

The unknown sensitivity variables, $\frac{\partial \phi}{\partial \theta_j} = \nabla_{\theta_j} \phi$, can be expressed in matrix form as a linear algebraic problem given in Eq. 6.

$$\nabla_{\phi} h \cdot \nabla_{\theta_j} \phi = -\nabla_{\theta_j} h \qquad j = 1 \ldots N \tag{6}$$

The $M \times M$ dimensional matrix $\bigtriangledown_{\phi} h$ contains the derivatives of the transport equations with respect to the state variables. The righthand side vector $-\bigtriangledown_{\theta_j} h$, represents the partial derivatives of transport equations according to parameters. The same derivative matrix $\bigtriangledown_{\phi} h$ also appears in the transport problem when solving with Newton's methods. Thus, the state Jacobian matrix $\bigtriangledown_{\phi} h$ has to be factorized once to obtain the sensitivity information. For the discretized PDE constraints, special solvers like LU decomposition can compute sensitivity information easily by linear algebraic operations (LU-Backsubstitution). The implementation of case studies did not reuse the factorization of the state Jacobian, $\bigtriangledown_{\phi} h$, because an iterative matrix-free Newton-Krylov method[22] is applied to solve linear algebraic equations.

Adjoint variables offer an alternative method for reducing the computational expense of computing gradients.[23] Adjoint

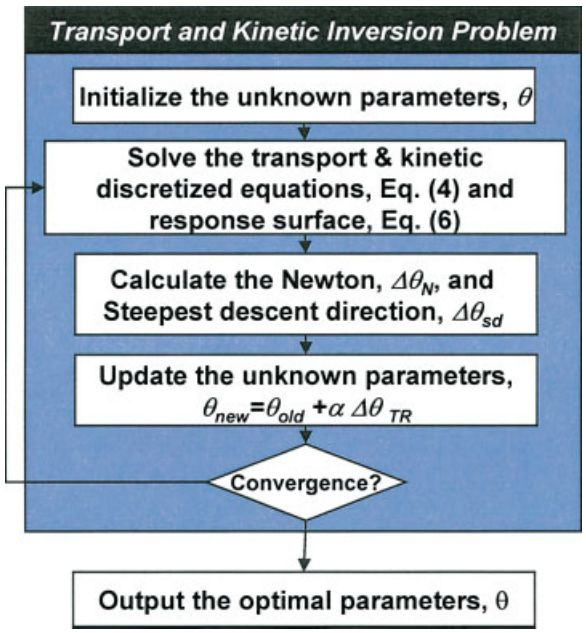

Figure 2. Overall flowsheet of solving TKIP in reduced parameter space and sensitivity maps.

[Color figure can be viewed in the online issue, which is available at www.interscience.wiley.com.]

methods are advantageous for problems with a large number of unknown parameters. However, when there are relatively few optimization parameters, sensitivity maps describing the influence of the design parameters on the states of the transport systems are more attractive. Furthermore, sensitivity maps provide a way to quantify the statistical information of the optimal parameters from experimental data.

The next section introduces a robust mathematical programming formulation for the solution of large-scale *TKIPs*.

Mathematical Solution Approaches for TKIP

After discretizing the PDE constraints, the transport and kinetic inversion (TKIP) problem of distributed systems and its boundary conditions can reformulated as shown in Eqs. 7 and 8. This nonlinear program is hard to solve because of its size and the coupling between the algebraic equations resulting from spatial discretization of the partial-differential equations.

$$\min_{\theta,\phi} \psi(\theta) = (\phi(x,t,\theta) - \hat{\phi}(x,t))^T F^{-1} (\phi(x,t,\theta) - \hat{\phi}(x,t)) \quad (7)$$

s. t.

$$h(\phi,\theta) = 0 \quad (8)$$

A specific challenge in inversion problem of distributed system arises from the iterative improvement of the parameter set θ. Large parameter corrections may transcend physically meaningful ranges, causing divergence of the overall procedures. To circumvent convergence problems, we propose an inexact trust region method with the following advantages: (i) the parameter set is bounded in each iteration; (ii) first and second response maps provide the necessary gradient and Hessian information, and (iii) sparse matrix implementations permit a very efficient treatment of the large-scale equality constraints stemming from the discretized-transport phenomena.

We will propose a reduced space search in which a transport problem is solved in each optimization loop as outlined in Figure 2. We will show that our solution approach will iterate over a sequence of optimization problems with largely reduced number of optimization variables. In each iteration, the global error surface is approximated by a multivariable Taylor expansion of the state variables ϕ, with respect to the parameters θ. This approximation incurs linear subproblems when using first-order sensitivity information, or quadratic problem with second-order response maps. More detailed information can be found elsewhere.[24] Alternatively, we have tested a simultaneous full-space solution with trust region, SQP or rSQP method.[25–27] In addition, we propose the advantage of using inexact methods to speed TKIP convergence. The inexact evaluation of the system and its sensitivity information will be obtained by a matrix-free Newton-Krylov method[22] and is discussed next.

Implementation: Inexact trust region method

The trust-region method is a gradient-based nonlinear optimization algorithm with step-size control. It chooses the search direction as a combination of the Newton and the steepest descent directions as shown in Figure 3a. This combination

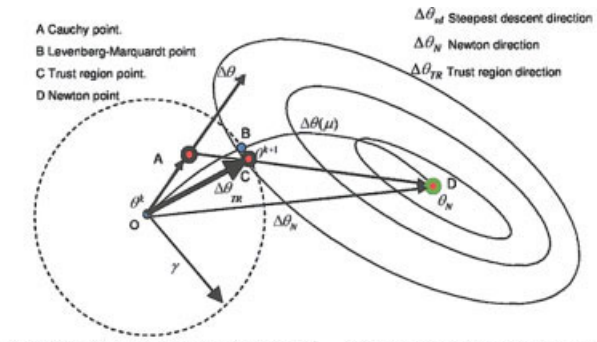

(a) Trust region. The trust region step, $\Delta\theta_{TR}$, is a linear combination of the Newton, $\Delta\theta_N$, and steepest descent, $\Delta\theta_{sd}$, direction inside the trust region sphere of radius, γ.

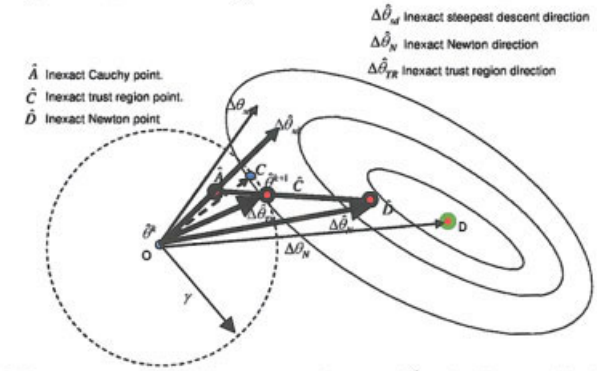

(b) Inexact trust region. The inexact trust region step, $\Delta\hat{\theta}_{TR}$, is a linear combination of the inexact Newton, $\Delta\hat{\theta}_N$, and an inexact steepest descent, $\Delta\hat{\theta}_{sd}$, direction.

Figure 3. Trust region method with exact and inexact information of the steepest descent and Newton directions.

[Color figure can be viewed in the online issue, which is available at www.interscience.wiley.com.]

affords it the crucial advantage that it can be applied even when the Jacobian and Hessian matrices are singular or near singular. This feature is important in many ill-conditioned transport and kinetic inversion problems. Its name "trust region" derives from the concept of a user-defined scalar that is, γ. It measures the maximum permissible change in parameter estimation updates ($\|\Delta\theta\| \leq \gamma$) from one iteration to another.

However, it is not necessary to solve the large-scale discretized PDEs constraints and their derivative information exactly when far away from the final solution. An inexact implementation of the trust region method is proposed to accelerate the computational approach, while maintaining the robustness of the trust region method. Suppose that PDEs constraints (2) of TKIP are not solved exactly, but only approximations of the node $\tilde{\phi}$, and sensitivity information $\frac{\partial\tilde{\phi}}{\partial\theta}$, are computed as shown in Figure 3b. The inexact trust region method could be formulated as Eqs. 9 and 10.

$$\min_{\Delta\theta} \tilde{\psi}(x, \theta^k + \Delta\theta) = \left(\tilde{\phi}(x, \theta^k) + \tilde{J}(\theta^k) \cdot \Delta\theta - \hat{\phi}(x)\right)^2 \quad (9)$$

s. t.

$$\|\Delta\theta\| \leq \gamma \quad (10)$$

The proposed inexact trust region method uses approximation for the state $\hat{\phi}$, and the sensitivity $\tilde{J} = \frac{\partial\hat{\phi}}{\partial\theta}$, but is otherwise identical to the traditional trust region method.

What are the accuracy requirements on evaluations of functions and derivative information? To keep the strong global convergence for the inexact trust region method, the relative error of the Jacobian $\tilde{J}$, has to be bounded in each iteration. Some researchers have shown global convergence of the inexact trust region algorithm provided that the relative gradient error satisfies Eq. 11[28,29]

$$\frac{\|e_k\|}{\|g_k\|} \leq \zeta \quad (11)$$

The expression $\|e_k\|$ is the norm of residual errors of the discretized transport and sensitivity functions in each iteration. The scalar $\|g_k\|$, represents the first-order derivative of the least-square objective function, which is $(\phi(x, \theta^k) - \hat{\phi}(x))^T \tilde{J}$. The user-specified constant ζ has a typical value 0.8.[28] The information flow for the inexact trust region method is summarized in Table 1. The first step calculates the residual error and sensitivity of the functions according to inexact error control. Then, we calculate the steepest descent direction $\Delta\theta_{sd}$, Cauchy point with optimal acceleration β and Gauss-Newton step. The second step determines a suitable direction by comparing the trust region radius with length of the Cauchy step and Gauss-Newton step. The third step performs the variable and functions update. If the new residual error is not reduced $\psi(\theta^{k+1}) > \psi(\theta^k)$, we can do line search and update the trust region radius γ. If the total residual error decreases $\psi(\theta^{k+1}) < \psi(\theta^k)$, there are three alternatives for choosing a new trust region radius γ. The choice of doubling, halving or retaining the current radius is determined as a function of the actual and predicted error reduction. These properties and linesearch guarantee the global convergence of the inexact trust region method.[30,31]

The next section will serve as motivating examples for TKIP. Their solution also demonstrates current capabilities of computer based methods. The first problem introduces an image reconstruction problem. It will demonstrate how to quantify metabolic activity of neurotransmitter and drug transport in the human brain from medical images. Second, the recovery of the thermal properties in Plutonium oxide storage vessel involves a 2-D inversion problem with reaction, convection and radiation. The third problem solves for the kinetic rates and diffusivities in a catalytic pellet reactor. The catalytic reactor is a dynamic distributed inversion problem with multiple-length scales.

Table 1. The algorithm of Inexact Trust Region Method

Give initial guesses for the unknown parameters, θ^0, and trust region radius $\gamma = 0.4$
Do:
Solve the distributed model Eq. 5 and its sensitivity equation Eq. 6 inexactly.
Calculate $\Delta\hat{\theta}_{sd}$, β and $\Delta\hat{\theta}_N$, where $\beta = \frac{\|\Delta\hat{\theta}_{sd}\|}{\|J\cdot\Delta\hat{\theta}_{sd}\|}$
Repeat:
if: $\gamma \leq \beta\|\Delta\hat{\theta}_{sd}\|$, *then:* $\Delta\hat{\theta} = \gamma\Delta\hat{\theta}_{sd}/\|\Delta\hat{\theta}_{sd}\|$ "Cauchy point outside trust region"
Else if: $\gamma \geq \|\Delta\hat{\theta}_N\|$, *then:* $\Delta\hat{\theta} = \Delta\hat{\theta}_N$. "Gauss-Newton inside trust region radius"
Else: $\|\Delta\hat{\theta}_N\| < \gamma < \beta\|\Delta\hat{\theta}_{sd}\|$, *then:* $\Delta\hat{\theta} = \eta\Delta\hat{\theta}_N + (1-\eta)\beta\Delta\hat{\theta}_{sd}$, where $\eta = (\gamma - \beta\|\Delta\hat{\theta}_{sd}\|)/(\|\Delta\hat{\theta}_N\| - \beta\|\Delta\hat{\theta}_{sd}\|)$. "Trust region radius between Cauchy point and Gauss-Newton point"
End
Update $\theta^{k+1} = \theta^k + \Delta\hat{\theta}$.
Determine whether θ^{k+1} is acceptable by checking whether $\|\psi(\theta^{k+1})\| < \|\psi(\theta^k)\|$, and calculated a new value of γ.
Until θ^{k+1} is an acceptable next point.

Applications and Computational Results

In this section, we will present three case studies to demonstrate optimization algorithms to extract the optimal parameters from distributed experimental data. The detailed geometry, computational grid and boundary conditions of each case study can be found in Table C1 in Appendix C. In this article, the number of finite volumes is fixed and obtained from repetitive simulations until the results of simulation did not depend on the number of grid elements.

Discovery of cerebral transport and metabolic reaction properties

Novel high-resolution imaging techniques, such as functional magnetic resonance imaging (fMRI), diffusion tensor imaging (DTI), and positron emission tomography (PET), have improved medical diagnosis. Unfortunately, existing imaging techniques are mainly used qualitatively for diagnosis. We propose to recover quantitative information, such as transport or metabolic reaction properties of a drug from these advanced images.

The *simultaneous identification of metabolic and transport properties from medical images* has not been reported in the literature before. As an example considers dopamine a neurotransmitter responsible for regulating a metabolic cascade to control critical cognitive functions. Figure 4 depicts the simplified metabolic pathway for fluorescent Fdopa from the blood circulation (plasma) into the brain tissue obtained *in vivo*.[32] Following injection into the blood circulation, Fdopa diffuses from the blood into the brain according to rate of blood-tissue clearance K_1, and back into the blood with a relative rate of tissue-blood clearance k_2. Fdopa can form methyl-

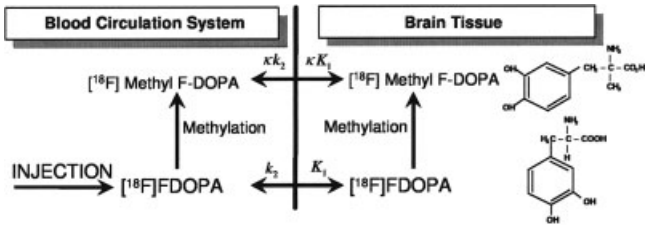

Figure 4. Pathway of Fdopa in the plasma circulation and brain tissue.

Fdopa which also traverse between the vascular system and the brain. Finally, residual Fdopa can be cleared into cerebrospinal fluid from where it returns to the venous circulation.

In this article, a simplified diffusion-clearance model is presented to quantify the transport and clearance of Fdopa in the brain tissue and in blood circulation using *TKIP*. The distribution of radiolabeled Fdopa can be measured with positron emission tomography (PET) *in vivo*.[32] The color intensity of the PET image reveals Fdopa distribution in the midbrain as depicted in Figure 5a in a horizontal cut of the human brain. The aim of the *TKIP* approach is to quantify the rate of tissue to blood clearance k_2, and blood to tissue clearance parameter K_1, of Fdopa and methyl-Fdopa. In addition, the diffusivities D_D, D_M, will be determined. The extravascular concentration of Fdopa in the brain tissue in the absence of metabolism is determined by Eq. 13. The extravascular concentration of methyl-Fdopa is determined by Eq. 14. The TKIP for the diffusion-clearance model of F-DOPA can be formulated as given in system (Eqs. 12–14).

$$\min_{D,K_1,k_2,C} \psi(D,K_1,k_2) = \left(C(x)-\hat{C}(x)\right)^T F^{-1}\left(C(x)-\hat{C}(x)\right) \quad (12)$$

s. t.

$$\nabla(D_D \nabla C_D) = K_1 C_a - k_2 C_D \quad \text{Fdopa clearance} \quad (13)$$

$$\nabla(D_M \nabla C_M) = \kappa K_1 C_m - \kappa k_2 C_M \quad \text{methyl} - \text{Fdopa clearance} \quad (14)$$

In Eq. 14, κ denotes the ratio rate of blood-tissue clearance. An accurate computational grid was constructed from the PET image depicted in Figure 5a using image reconstruction tools. The resulting unstructured computational grid is shown in Figure 5b. By interpreting the concentration profiles obtained *in vivo*, $\hat{C}$, the pixel color intensities were converted to concentration. The TKIP problem of Eqs. 12–14, was solved in generalized curvilinear coordinates on a Pentium IV 1.60 GHz with 1GB RAM, that required 2.3 min of CPU time. Figure 5c depicts the concentration field predicted for the optimal parameters set as shown in Table 2. While this case study used a simplified reaction network, it demonstrated the enormous potential of discovering metabolic and transport phenomena from medical images.

The next section introduces a thermal inversion problem in a Plutonium storage vessel.

Plutonium oxide storage tank

Plutonium waste needs to be stored in cylindrical containers for more than twenty years before final disposal. Due to nuclear decay, heat and gaseous by-products like Helium, are being generated causing a temperature and pressure rise in the container leading to risk of leakage and contamination. Risk analysis of this distributed system cannot be conducted in simplified benchmark experiments due to danger in material handling. Consequently, the coupled reaction and transport mechanisms have to be studied simultaneously inside the distributed cylindrical vessel. In addition, only limited temperature measurements as shown in Figure 6a, are available to quantify the unknown system properties, such as heat conduction, radiative-heat transfer and reactive-gas formation.[33–36] *Problem inversion* will extract unknown nuclear activity and transport parameters to assess the worst case temperatures in the storage vessel as shown in Figure 6a.

For discovering the heat source and heat transfer of PuO_2 tank, the inversion problem minimizes the least-squares errors between temperature measurements and model predictions as shown in Eqs. 15 and 16.

$$\min_{q,k_{eff},h_o,T} \psi(\theta) = [T(r,z)-\hat{T}(r,z)]^T F^{-1}[T(r,z)-\hat{T}(r,z)]$$

$$\theta = \{q, k_{eff}, h_o\} \quad (15)$$

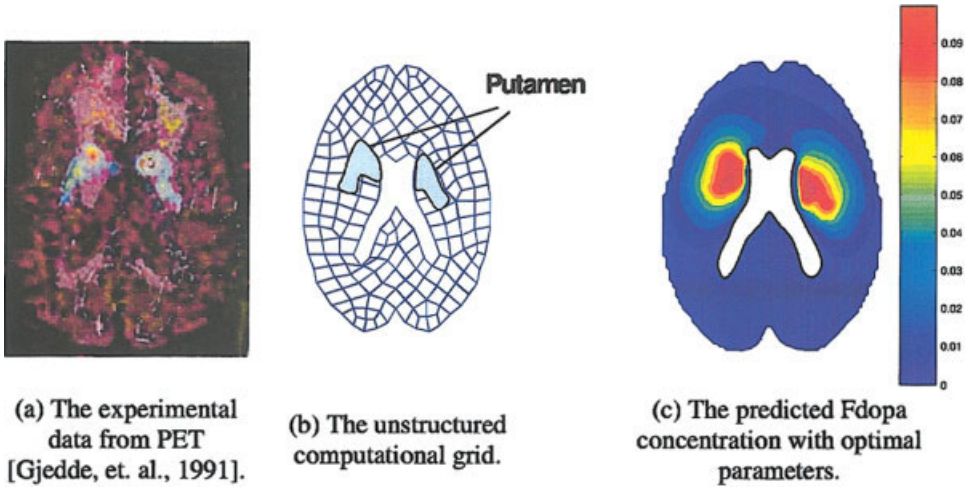

Figure 5. Results of solving TKIP for Fdopa distribution in human brain.

[Color figure can be viewed in the online issue, which is available at www.interscience.wiley.com.]

Table 2. Optimal Properties of Fdopa in Human Brain

Parameters	Optimal Value
Diffusivity of Fdopa, D_D	0.11×10^{-6} cm$^2 \cdot$s^{-1}
Diffusivity of methyl-Fdopa, D_M	0.15×10^{-6} cm$^2 \cdot$s^{-1}
Blood-tissue clearance of Fdopa, k_2	0.0042 s^{-1}
Tissue-blood clearance of Fdopa, K_1	0.0009 s^{-1}
κ	Set at 0.43 [Gjedde et al., 1991]

s. t.

$$h(T,q,k) = \nabla(\alpha\nabla T) + q|j^{-1}| = 0 \tag{16}$$

where α is the effective thermal conductivity, $\alpha = k_{eff} + \frac{16}{3}\frac{\sigma}{\alpha_R}T^3$; σ is the Stefan-Boltzmann constant, and α_R is the Rosseland mean absorption as shown in Table 3; q is the nuclear heat generation. The inversion problem Eqs. 15 and 16 with the heat and radiation equation was solved by proposed methodology. Figure 6b shows 2-D temperature distributions in plutonium storage tank, corresponding to the optimal parameters, q = 5383.2; $k_{eff} = 2.1$; $h_o = 8.7$. The worst case temperature lies on the main axis in the lower-part of the cylinder. Figure 6c describes the temperature profile along with the radius in different heights of vessel.

Risk analysis involves the identification of the worst case performance scenarios due to the uncertainty in the estimated parameter. The sensitivity information obtained during inversion problem permits the calculation of the probabilistic parameter ranges. Specially, we can construct *Individual Confidence Region* (ICR) and *Joint Confidence Region* (JCR) in the uncertain parameter space for any desired confidence level. Exact joint probability density functions can be obtained by the likelihood or lack-of-fit methods;[37] we propose linearized simpler ideas of ICR and JCR for computational economy. Eqs. 17–19 introduce the steps for calculating the covariance matrix $F_{\hat{\theta}}$. However, ICR and JCR are only approximation in the nonlinear case.[37–39] The covariance matrix $F_{\hat{\theta}}$, helps approximate probability density functions for uncertain parameter realizations. In flexible design, it is necessary to limit the range of relevant parameter variations. A finite range of possible parameter realization can be determined according to a chosen risk tolerance. The scalar confidence or α-*level* defines a cut-off point outside which the risk associated with highly unlikely parameter realization is deemed tolerable. After specifying appropriate confidence levels (like $\alpha = 0.99$), Eq. 18 delineates an *Individual Confidence Region* for each parameter Θ_j, according to its variance F_{jj}, and the outcome of a *student t-distribution*. Similarly, *Joint Confidence Region* for the parameters can be constructed according to Eq. 19. The joint confidence region has the advantage of accounting for cross-correlation among uncertain variables

$$F_{\hat{\theta}} \approx s^2\left(J(\hat{\theta})^T J(\hat{\theta})\right)^{-1} = \begin{pmatrix} \sigma_{11} & \cdots & \sigma_{1m} \\ \vdots & \ddots & \vdots \\ \sigma_{m1} & \cdots & \sigma_{mm} \end{pmatrix} \text{ where } s^2 = \frac{e^T e}{n-p} \tag{17}$$

$$|\theta_j - \hat{\theta}_j| \le F_{jj}^{1/2} t_{N-M,1-\alpha/2} \tag{18}$$

$$(\theta - \hat{\theta})^T F_{\hat{\theta}}^{-1}(\theta - \hat{\theta}) \le p \cdot F_{N,M-N,1-\alpha} \tag{19}$$

The variance-covariance matrix of three estimated parameters, heat source q, effective thermal conductivity coefficient k_{eff}, and heat-transfer coefficient h_o, introduced earlier, is given in Eq. 20

$$F_{\hat{\theta}} = \begin{bmatrix} 35.9 & 3.82 & 3.38 \\ 3.82 & 0.55 & 0.25 \\ 3.38 & 0.25 & 0.44 \end{bmatrix} \tag{20}$$

Accordingly, the individual variances for each parameter are the diagonal elements $\sigma_{11}^2 = 35.9$, $\sigma_{22}^2 = 0.55$ and $\sigma_{33}^2 = 0.44$. There is cross-covariance between the heat source and the heat-transfer coefficient according to the value of $\sigma_{13} = 3.38$. The correlation is not a surprise as both thermal properties are estimated from temperature measurements. Accordingly, the heat source, effective thermal-conductivity coefficient and the heat-transfer coefficient vary between $q = 5383.2 \pm 8.4$; $k = 2.1 \pm 0.47$; $h_o = 8.7 \pm 0.36$. Figure 7 depicts the 3-D visualization of the ellipsoidal-joint confidence region for a confidence level of 99.999%.

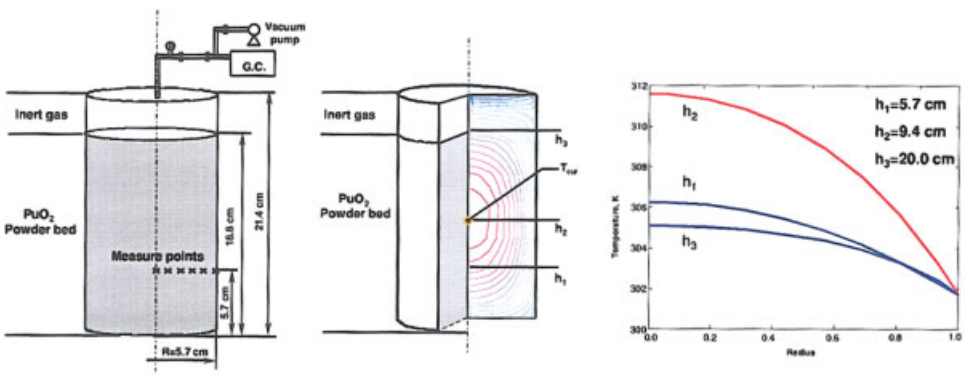

(a) Experimental setup of Plutonium storage vessel.

(b) Predicted temperature distribution with optimal parameter set.

(c) Temperature profile computed at different levels.

Figure 6. Temperature distribution with optimal parameters, q = 5383.2; k_{eff} = 2.1; h_o = 8.7 obtained by problem inversion of temperature measurement collected at five locations 5.7 cm from the bottom of the container.

[Color figure can be viewed in the online issue, which is available at www.interscience.wiley.com.]

Table 3. Physical Properties of the Plutonium Storage Vessel

- Radius (R_b) = 0.057 m
- Length (L_b) = 0.188 m
- The height at which the radial temperatures are measured = 0.057 m
- $\sigma = 5.67 \times 10^{-8}$
- $a_R = 8000$
- $T_a = 301.7$ K

The plutonium storage could be analyzed at steady state due to slow changes of the system properties. However, dynamics are important in fast processes, such as heterogeneous catalysis. In the next section, we will recover the transport and reaction properties in the steady and dynamic catalytic pellet reactor using the steady- and time-dependent observations.

Catalytic pellet reactor

The aim of this case study is to determine the reaction rate in catalyst pellets, diffusion and activation energy, as well as the resulting composition and temperature profile in the plug-flow reactor. The heterogeneous overall *reaction* stochiometry is given in Eq. 21. The *TKIP* will be solved for the steady and dynamic cases.

$$A \xrightarrow[\Delta H]{Catalyst} B \tag{21}$$

2-D reactor model with porous catalyst packing

The species and heat balance in axial and radial direction for a cylindrical control volume of the catalytic reactor filled with pellet packing as shown in Figure 8 are given in Eqs. 22 and 23.

$$\nabla(\vec{u}C_A) = \nabla(D_A \nabla C_A) + r_A|j^{-1}| \tag{22}$$

$$\rho_g C_p \nabla(\vec{u}T) = \nabla(k_e \nabla T) + r_A \Delta H|j^{-1}| \tag{23}$$

where r_A is the overall rate of reaction within the catalyst per unit mass of catalyst. Since the catalytic pellet reactor is filled with small catalytic pellets, the reactor content can be treated as porous material. The momentum transfer in the pellet reactor is approximated by Darcy's law as given in Eq. 24.

$$-\nabla P = \frac{\mu}{k_m}\vec{u} \tag{24}$$

The reactions in the bulk are coupled with the kinetics and mass transfer of the porous pellets via the effectiveness factor η. The effectiveness factor accounts for mass transfer and reaction inside the pellet expresses the overall reaction rate in terms of the surface concentration and pellet surface temperature. The expression of rate of reaction has been expressed by Arrhenius equation as shown in Eq. 25.

$$r_A = -\eta S_a k_{ref} \exp\left[-\frac{E}{RT_{ref}}\left(\frac{T_{ref}}{T} - 1\right)\right] C_A \tag{25}$$

S_a is the internal surface area of the pellet. The external effectiveness factor η relate the actual conversion in the pellet to a homogenous reference.[40] All constants are listed in Table 4. The effectiveness factor links the bulk conversion of reactant to the transport and catalytical reactions inside the pellet.

Catalytic Pellet Model. The catalytic pellets can be treated as a porous media with coupled reaction and heat transfer. The reactions in the pellet are assumed to be fast enough to justify steady-state assumption for the pellets. The fully coupled non-

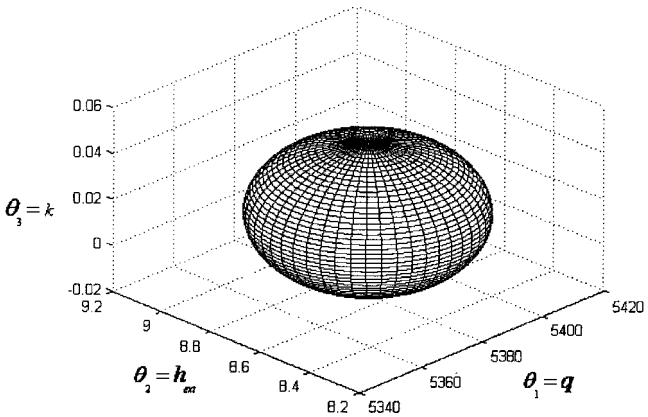

Figure 7. Joint confidence region for the parameters, heat source q, effective thermal-conductivity coefficient k_{eff}, and heat-transfer coefficient h_o, according to a confidence level of 99.999%.

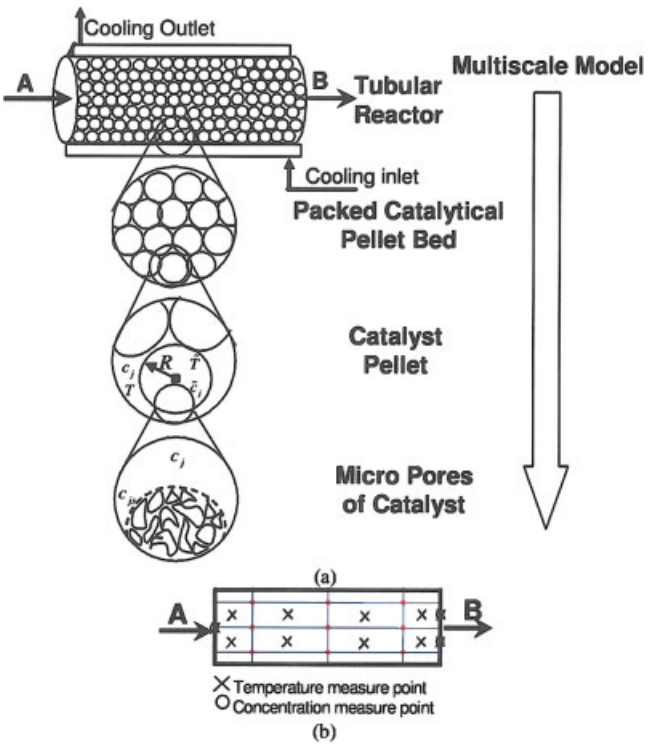

Figure 8. Multiple length scale of a catalytic pellet reactor (a), and measurements (b), to determine reaction, mass- and heat-transfer properties.

[Color figure can be viewed in the online issue, which is available at www.interscience. wiley.com.]

Table 4. Physical Properties of the Catalytic Pellet Reactor

Physical Properties of the Pellet
$\varepsilon = 0.4$ (porosity)
$D_e = 5.2 \times 10^{-6}$ m^2/s
$R_0 = 0.003$ m
$\rho_c = 2.8 \times 10^3$ Kg/m^3
Physical Properties of the Bed
$\varepsilon_b = 0.4$
$\rho_b = \rho_c(1 - \varepsilon_b)$
Physical Properties of the Inlet Gas
$C_{bo} = 1.6$ mol/m^3
Reaction Conditions
$\Delta H = 97200$ J/mol

isothermal concentration profile inside the pellet can be expressed in dimensionless form as Eq. 26, with boundary conditions (27):

$$\frac{d^2\tilde{C}_A}{dR^2} + \frac{2}{R}\frac{d\tilde{C}_A}{dR} - \Phi^2\tilde{C}_A \exp\left(\gamma\beta\frac{1-\tilde{C}_A}{1+\beta(1-\tilde{C}_A)}\right) = 0 \quad (26)$$

$$\tilde{C}_A = 1 \text{ and } \frac{d\tilde{C}_A}{dR}|_{R=0} = 0 \quad (27)$$

These dimensionless variables represent the Thiele modulus $\Phi^2 = \frac{R_0^2 k_0}{D_e}$, the species concentration $\tilde{C}_A = \frac{C_A}{C_0}$, radius $R = \frac{r}{R_0}$, activation energy $\gamma = \frac{E}{R_g T_0}$ and heat generation $\beta = \frac{C_0 \Delta H D_e}{k_e T_0}$.[41,42] When the mass-and heat-transfer resistance across the boundary layer is small, the bulk and surface conditions are the same. Then, C_0 and T_0 are taken to be the concentration of reactant and temperature on the surface of the pellet. Eq. 27 shows that reactant concentration and temperature at pellet surface are equal to bulk flow. At the center of the pellet, there is no mass and heat flux $\frac{d\tilde{C}_A}{dR} = 0$. The orthogonal collocation on finite elements is employed to solve for $\tilde{C}_A$ in each volume.[43] Figure 9 displays the dimensionless-concentration distribution in catalytic pellets.

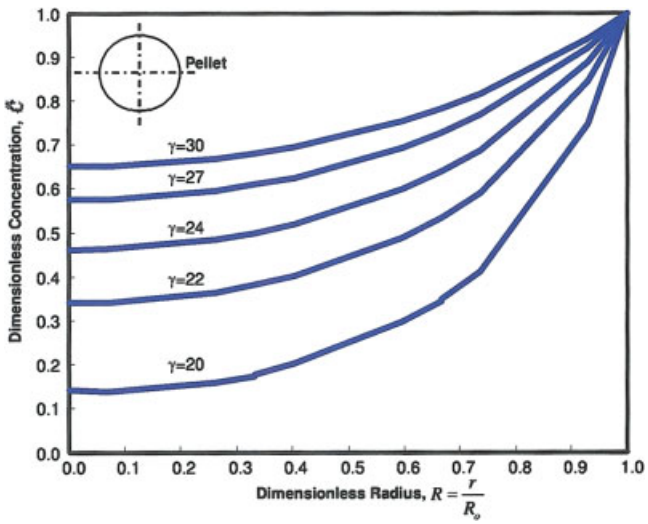

Figure 9. Concentration profiles of catalytic pellet solved by the orthogonal collocation on finite elements with different dimensionless activation energies ($\gamma = E/R_gT_0$).

[Color figure can be viewed in the online issue, which is available at www.interscience.wiley.com.]

Inversion of Kinetic Experiments. The concentrations of reactants are measured at inlet and outlet of the reactor. Temperatures are easily obtained at different locations along the reactor. With measured inlet and outlet concentration, and the temperatures inside the reactor the diffusivity of reactor D_{AB}, reaction constant k_{ref}, and activation energy E, were determined according to the inversion problem (Eq. 27).

$$\min_{D_{AB},k_{ref},E_a,C,T} \psi(\theta) = \left(\begin{bmatrix} C \\ T \end{bmatrix} - \begin{bmatrix} \hat{C} \\ \hat{T} \end{bmatrix}\right)^T F^{-1} \left(\begin{bmatrix} C \\ T \end{bmatrix} - \begin{bmatrix} \hat{C} \\ \hat{T} \end{bmatrix}\right) \quad (28)$$

s. t. Eqs. 22–26

The optimal parameters were found to be $D_{AB} = 1.28 \pm 0.16 \times 10^{-5}$ (m^2/s); $k_{ref} = 9.14 \pm 0.38 \times 10^{-5}$ (1/s); and $E = 5281 \pm 35.9$ (J/mol). In this case, we are able to predict the concentration distribution from the temperature distribution. Figure 10 illustrates the convergence paths for the diffusivity and reaction parameters from two different initial guesses. Multiple solutions occur frequently in kinetic inversion problems, when the experimental measurements have errors. In the case studies, measurement error had a variance of 5%. It is a considerable challenge to identify the true solution from the multiple local optima. A naïve approach would always declare the global minimum as the true solution. However, this global residual error minimum is not guaranteed to be physically better than other local minima.[24]

Dynamic Analysis. We also use the dynamic data to analysis transient performance of pellet reactor. We inverted the dynamic data obtained in response to a concentration step change as listed in Table 5. Figure 11 displays the dynamic evolution of concentration and temperature profiles with respect to time. We also expect much better accuracy in temperature dependent data for the activation energy E than ones from steady-state data. This case study demonstrates that our proposed methodology is capable of solving dynamic inversion problem.

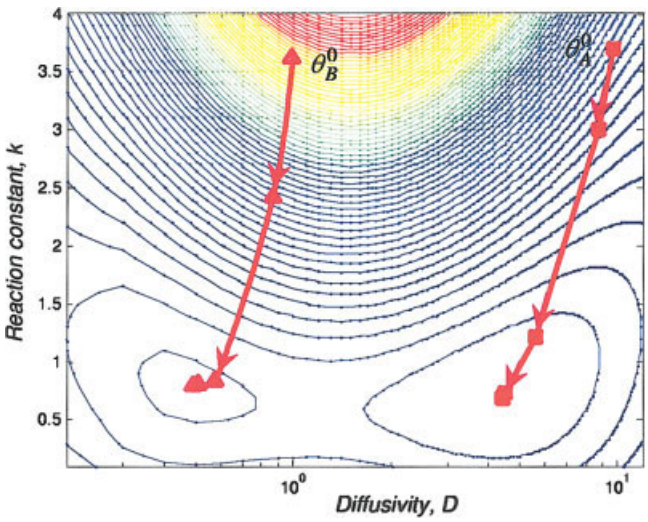

Figure 10. Convergence trajectory of transport and kinetic inversion of the reactor dynamics.

[Color figure can be viewed in the online issue, which is available at www.interscience.wiley.com.]

Table 5. Dynamic Temperature Measurements in the Catalytic Pellet Reactor

Time (s)	Temperature (K) $r = 0.375$, $z = 0.2$	$r = 0.375$, $z = 0.56$	$r = 0.375$, $z = 0.94$
1	306.9	298.2	298.1
2	344.5	300.7	298.2
4	390.6	307.6	298.9
6	465.3	324.5	302.6
9	568.5	356.8	313.3
15	663.8	401.0	329.4
23	715.8	438.0	342.6
40	729.2	451.8	347.8
78	730.7	453.7	348.7
100	730.7	453.7	348.7

r, dimensionless radius, z, dimensionless length from entrance.

Computational Performance of Problem Inversion

The numerical solution of the TKIP poses a formidable challenge. Several gradient-based optimization routines were investigated for performance and robustness. The performance results are summarized in Table 6. All solvers were implemented in Pentium IV 1.60 GHz with 1GB RAM.

Simultaneous Solutions. For the solution of the nonlinear programming, we tested the Trust Region solver (MINPACK),[44] SQP, rSQP[45–47] to solve the problem simultaneously using analytical Jacobian information, as well as results obtained by numerical differentiation. To comparison, the implementation of the proposed algorithm had the same structure with Trust Region solver in MINPACK. We investigated those methods for the direct full-size solution of the inversion problem as described in system 1 and 2. Accordingly, the unknown estimation parameters, and all state variables were open variables. For the reactor problem, the simultaneous programming succeeded with analytical Jacobians, but failed often with numerically differentiated derivative information. All computational results were obtained in less than thirty iterations. The solution of the transport equations and their sensitivity equations in each iteration consumes the largest amount of computational time. For problems with many parameters, the numbers of first and second sensitivity equations increases. In those cases, adjoint methods might be considered.

Reduced Space Solutions. Trust region and inexact trust region are used to solve for TKIP. We found the proposed inexact trust region method to be robust as long as analytical derivatives were used to obtain the sensitivity information. Its performance was reasonable and compared with other methods. We did not find significant performance difference between the full and the reduced space approaches.

Second-Order Sensitivity Information. Numerical optimization methods requiring Hessian information often circumvent second-order numerical differentiation by updating cleverly first-order sensitivity information, BFGS update. However, secant-based Hessian approximations can lead to failure of transport and kinetic inversion problem. On the other hand, the relatively simple problem structure and the sparsity pattern of transport equations stemming from the finite volume discretization makes analytical approaches to acquire second-order sensitivity information attractive.[4,48] We propose to exploit second-order information for improving the robustness and convergence of the inexact trust-region method. Given first-order sensitivity information as shown in the Mathematical Treatment of the Transport Equations section, second-order expressions $\frac{\partial^2 \phi_i}{\partial \theta_i \partial \theta_j}$, can be calculated by differentiating Eq. 5 with the chain rule to obtain Eq. 29.

$$\nabla_\phi h \cdot \nabla_{\theta_i} \nabla_{\theta_j} \phi = -[\nabla_\phi \nabla_\phi h \cdot \nabla_{\theta_j} \phi + \nabla_\phi \nabla_{\theta_j} h] \cdot \nabla_{\theta_i} \phi - \nabla_\phi \nabla_{\theta_i} h \cdot \nabla_{\theta_j} \phi - \nabla_{\theta_i} \nabla_{\theta_j} h \quad (29)$$

The second-order sensitivity information $H = \frac{\partial^2 \phi_i}{\partial \theta_i \partial \theta_j}$, can be calculated by solving $N \times N \times M$ linear algebraic equations in Eq 29. Then, the trust region method can be augmented with additional second-order term according to Eqs. 30 and 31

$$\min_{\Delta\theta} \tilde{\psi}(x, \theta^k + \Delta\theta) = \left(\tilde{\phi}(x, \theta^k) + \tilde{J}\Delta\theta + \frac{1}{2}\Delta\theta^T \tilde{H} \Delta\theta - \hat{\phi}(x) \right)^2 \quad (30)$$

s. t.

$$\|\Delta\theta\| \leq \gamma \quad (31)$$

Computational results with second-order sensitivity

We tested the second-order trust region method for the catalytic-pellet reactor. We found that the convergence still can be

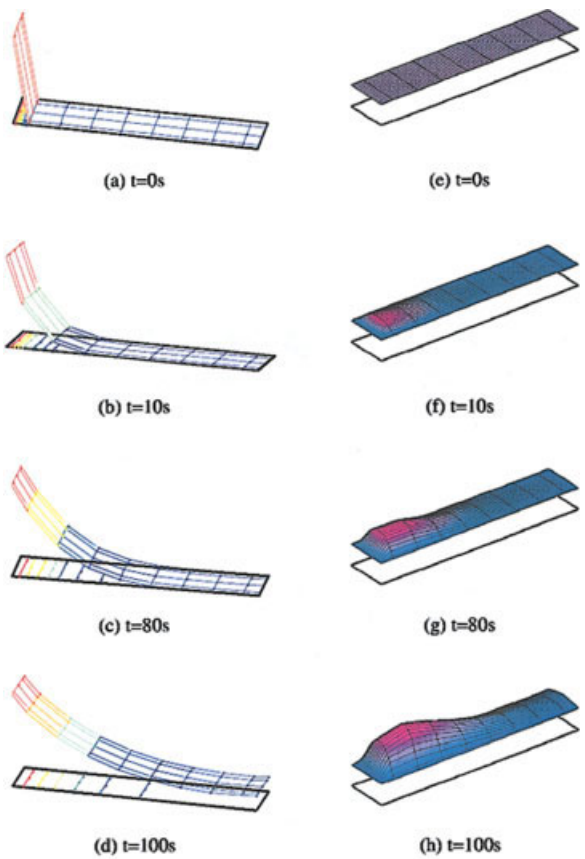

Figure 11. Evolution of concentration (a–d) and temperature (e–h) fields varied with time.

[Color figure can be viewed in the online issue, which is available at www.interscience.wiley.com.]

Table 6. Comparison of Performance of Different Numerical Methods

		Simultaneous approach						Reduced space approach			
		Trust region		SQP		rSQP		Trust region		Inexact trust region	
CPU time		FD	A	FD	A	FD	A	FD	A	FD	A
Simultaneous approach	Case 1	14.8 min	9.4 min	12.4 min	7.3 min	8.3 min	4.8 min	Fail	3.1 min	Fail	2.3 min
	Case 2	21.8 min	11.8 min	18.8 min	9.8 min	12.5 min	6.8 min	Fail	6.2 min	Fail	5.7 min
	Case 3	Fail	13.8 min	Fail	10.2 min	Fail	8.2 min	Fail	7.9 min	Fail	6.1 min

Note: FD: finite difference; A: Analytical.

obtained even when the artificial white noise of experimental data was 20%, while all algorithms with only first-order sensitivity failed. Moreover, the minimum weight least-square error increased from 0.657 to 4.759. This non-zero residual error also demonstrated the needs of the second-order sensitivity information for sufficient numerical performance. The computation time of inversion problem with second-order sensitivity information is 3 min longer due to additional cost for computing $\frac{\partial^2 \phi_i}{\partial \theta_i \partial \theta_j}$ by the $N \times N \times M$ linear algebraic equations (Eq. 29). However, the overall computation time did not increase dramatically due to application of inexact sparse solver and the reduction of update steps. Moreover, in this preliminary implementation, we did not exploit advantages in reusing the factorization of the state Jacobian $\bigtriangledown_{\phi} h$. This additionally expected features would further decrease the cost for constructing second-order response surfaces.

Conclusion and Significance

We have proposed a reliable numerical optimization approach to discover unknown diffusion and convection phenomena as well as chemical reaction rates from observed concentration or/and temperature measurements in distributed systems. The finite volume method was used to discretize the distributed-transport equations. The generalized coordinate transformation defined over unstructured grids enables problem inversion for domain of arbitrarily complex shape. We propose an inexact trust region mathematical programming method, and first-or second-response maps to improve the robustness and convergence of large-scale PDE optimization problems. Optimal physical parameters were obtained in three different case studies to demonstrate the efficiency of the proposed methodology. The resulting optimization problem also handles large problem sizes very effectively in terms of their time and space complexity with the help of sparse matrix technique. The proposed problem formulation searches in a reduced parameter space; this feature will make problem inversion amenable enable to global terrain optimization algorithm.[49] The global terrain methods will help identify all solutions of the inversion problem; this work is planned as future research.

Different mathematical programming approaches and their strengths were assessed and compared for their suitability in *transport and kinetic inversion problems*. We find the analytical techniques to acquire sensitivity information are necessary for ensuring robust convergence of numerical algorithms. This is especially important with noisy experimental data. The kinetic inversion problem in the transport distribution system for human brain has not been reported so far. It is expected that our results encourage the community to tackle the more distributed inversion problems in biology, chemical and nano systems.

It would be interesting to identify the global minimum for TKIP using existing global approaches.[50–55]

Notation

a_p, b_p = transport coefficients at current volume
a_E, a_W, a_N, a_S = east, west, north and south transport coefficients of the
b_E, b_W, b_N, b_S neighbors of the current volume
Bi_M = Biot number for mass transfer
C = concentration of reactant, mol/m^3
$\hat{C}$ = experimentally obtained concentration of reactant, mol/m^3
C_D = Dopa concentration in the tissue, mol/m^3
C_a = Dopa concentration in the blood system, mol/m^3
C_M = Methyl-Dopa concentration in the tissue, mol/m^3
C_m = Methyl-Dopa concentration in the blood system, mol/m^3
C_p = heat capacity of gas reactant, J/K
D_{AB} = mass diffusion coefficient, m^2/s
D_D, D_M = diffusion coefficients for Dopa and Methyl-Dopa, m^2/s
E = Arrhenius activation energy, J/mol
$\|e_k\|$ = norm of residual errors
F = variance – covariance matrix
$\|g_k\|$ = first-order derivative of the least square objective function
h = heat transfer coefficient, $J/(K{\cdot}s{\cdot}m^2)$
$h(x, \theta, \varphi)$ = set of equality constrains – set of transport equations
h_0 = heat transfer coefficient at the walls of the plutonium tank, $J/(K{\cdot}s{\cdot}m^2)$
H_D, H_T = source term in the transport equations accounting for the inclination of the faces in the balance envelope
$|J^{-1}|$ = determinant of the inverse Jacobian of the transformation
k = reaction constant, $1/s$
K_1 = tissue clearance parameter, $1/s$
k_2 = rate of tissue to blood clearance, $1/s$
k_e = heat conductivity, $J/(K{\cdot}s)$
k_{eff} = effective thermal conductivity of plutonium powder, $J/(K.s)$
k_m = permeability, m^2
k_{ref} = reaction constant at reference temperature, $T_{ref} = 298.3\ K$
M = number of state variables
N = number of unknown parameters
q = heat source, W/m^3
q_1, q_2, q_3 = geometric auxiliary properties
r = radial position, m
R = scaled radius, m
R_o = pellet radius, m
r_A = overall rate of reaction
S = source term
S_a = pellet internal surface area, m^2/Kg
T = temperature, K
$\hat{T}$ = experimentally obtained temperature, K
u = x-component velocity, m/s
v = y-component velocity, m/s
U = contravariant velocity, m/s
V = contravariant velocity, m/s
$x_\xi, y_\xi, x_\eta, y_\eta$ = metrics of the transformation
z = length, m

Greek letters

α = thermal conductivity that includes radiation
a_R = Rosseland mean absorption coefficient
γ = dimensionless variable in pellet equation
Γ = unknown transport coefficient e.g. diffusivity, viscosity, and so on
ΔH = heat of reaction, *J/mol*
ζ = user specified constant
η = effectiveness factor
θ = parameter set
κ = ratio of blood-tissue clearance
μ = viscosity, $Kg/(m{\cdot}s)$
ξ, η = generalized curvilinear coordinates
ρ = density, Kg/m^3
σ = Stefan-Boltzmann constant
φ = Scaled pellet concentration
Φ = thiele modulus
ϕ = unknown transport quantities
$\hat{\phi}$ = experimentally obtained transport quantities
ψ = error function

Subscripts

A = reaction substrate
b = bulk properties of the bed
D = Fdopa
g = reactant gas
M = methyl-Fdopa
nb = the neighbor volumes
p = current volume

Literature Cited

1. Hwang JY, Park C, Huang M, Anderson T. Numerical procedure to extract physical properties from Raman scattering data in a flow reactor. *J of the Electrochem Soc*. 2005;152:C334.
2. Akcelika V, Birosb G, Ghattasa O, Longc KR, Waanders BB. A variational finite element method for source inversion for convective–diffusive transport. *Finite Elements in Analysis and Design*. 2003;39:683.
3. Biegler L, Ghattas O, Heinkenschloss M, Waanders BB. Large-scale PDE-constrained optimization, Lecture notes in computational science and engineering. New York: Springer-Verlag; Vol. 30:2003.
4. Hakami A, Odman MT, Russell AG. High-order, direct sensitivity analysis of multidimensional air quality models. *Environ Sci Technol*. 2003; 37:2442.
5. Le Dimet FX, Navon IM, Daescu DN. Second-order information in data assimilation. *Monthly Weather Review*. 2002;130:629.
6. Ozisik MN, Orlande HRB, Inverse heat transfer. New York: Taylor and Francis; 2000.
7. Biros G, Ghattas O. Inexactness issues in the Lagrange-Newton-Krylov-Schur method. In: Biegler L, Ghattas O, Heinkenschloss M. Waanders BB. *Large-scale PDE constrained optimization. Lecture notes in computational science and engineering*. New York: Springer-Verlag; 2003.
8. Biros G, Ghattas O. Parallel Lagrange-Newton-Krylov-Schur methods for PDE-constrained optimization. Part I: The Krylov-Schur solver. *SIAM J on Scientific Comp*. 2005;27:687.
9. Biros G, Ghattas O. Parallel Lagrange-Newton-Krylov-Schur methods for PDE-constrained optimization. Part II: The Lagrange-Newton solver, and its application to optimal control of steady viscous flows. *SIAM J on Scientific Comp*. 2005;27:714.
10. Borggaard J, Burns J. A PDE sensitivity equation method for optimal aerodynamic design. *J of Comp Phys*. 1997;136:366.
11. Roy R, Sevick-Muraca EM. Truncated Newton's optimization scheme for absorption and fluorescence optical tomography: Part I theory and formulation. *Optics Express*. 1999;4:353.
12. Date AW. Introduction to computational fluid dynamics. New York: Cambridge University Press; 2005.
13. Patankar SV. *Numerical heat transfer and fluid flow*. Washington: Hemisphere Publishing Corporation; 1980.
14. Fletcher C. Computational techniques for fluid dynamic (Vol. I & II). New York: Springer-Verlag; 1991.
15. Linninger AA, Somayajı RMB, Xenos M, Kondapalli S, Zhu DC, Penn R. Drug delivery into the human brain", *Proceeding of Foundations of Systems Biology and Engineering. Corwin Pavilion*, Univ. of California Santa Barbara Campus; 2005:163.
16. Khinast JG. Impact of 2-D bubble dynamics on the selectivity of fast gas-liquid reactions. *AIChE J*. 2001;47:2304.
17. Saltelli A, Chan K, Scott M. *Sensitivity analysis*. New York: John Wiley & Sons; 2000.
18. Li S, Petzold LR. Software and algorithms for sensitivity analysis of large-scale differential algebraic systems. *J Comp Appl Math*. 2000;125:131.
19. Lei JR, Kramer MA. Sensitivity analysis of systems of differential and algebraic equations. *Comput Chem Eng*. 1985;9:93.
20. Frenklach M, Wang H, Rabinowitz MJ. Optimization and analysis of large chemical kinetic mechanisms using the solution mapping method: Combustion of methane. *Prog Energy Combust Sci*. 1992;18:47.
21. Caracotsios M, Stewart WE. Sensitivity analysis of initial value problems with mixed ODEs and algebraic equations. *Comput Chem Eng*. 1985;9:359.
22. Barrett R, Berry M, Chan TF, Demmel J, Donato J, dongarra J, Eijkhout V, Pozo R, Romine C, van der Vorst H. *Templates for the solution of linear systems: Building blocks for iterative methods*. SIAM Press; 1994.
23. Ozyurt DB, Barton PI. Large-scale dynamic optimization using the directional second-order adjoint method. *Ind Eng Chem Res*. 2005;44: 1804.
24. Tang W, Zhang L, Linninger AA, Tranter R, Brezinsky K. Solving kinetic inversion problems via a physically bounded Gauss-Newton (PGN) method. *Ind Eng Chem Res*. 2005;44:3626.
25. Arora N, Biegler LT. Parameter estimation for a polymerization reactor model with a composite-step trust-region NLP algorithm. *Ind Eng Chem Res*. 2004;43:3616.
26. Arora N, Biegler LT. A trust region SQP algorithm for equality constrained parameter estimation with simple parameter bounds. *Comput Optim Appl*. 2004;28:51.
27. Kameswaran S, Biegler LT, Staus GH. Dynamic optimization for the core-flooding problem in reservoir engineering. *Comput Chem Eng*. 2005; 29:1787.
28. Carter RG. On the global convergence of trust region algorithms using inexact gradient information. *SIAM J Numer Anal*. 1991;28:251.
29. Heinkenschloss M, Vicente LN. *Analysis of inexact trust-region SQP algorithms*. *SIAM J Optim*. 2001;12:283.
30. Conn AR, Gould NIM, Toint PL. *Trust region methods*. Philadelphia: SIAM; 2000.
31. Dennis JE, Schnabel RB. *Numerical methods for unconstrained optimization and nonlinear equations*. Philadelphia: SIAM; 1996.
32. Gjedde A, Reith J, Dyve S, Le'gerG C, Guttman M, Diksic M, Evans A, Kuwabara H. Dopa decarboxylase activity of the living human brain. *Proc Natl Acad Sci USA*. 1991;88:2721.
33. Bielenberg PA, Prenger FC, Veirs DK, Jones GF. *Effects of pressure on thermal transport in plutonium dioxide powder. AIChE Annual meeting*; 2004.
34. Hensel S. *Thermal analysis of the 9975 package as a plutonium storage container*. Westinghouse Savannah River Company Report. WSRC-TR-98-00203;1998.
35. Knight TD, Steinke RG. Thermal analysis of plutonium materials in British Nuclear Fuels, Ltd., containers, Los Alamos National Laboratory Report. LA-UR-97-1866; 1997.
36. Xu M, Abdou MA, Raffray AR. Thermal conductivity of a beryllium gas packed bed. *Fusion Eng and Design*. 1995;27:240.
37. Donaldson JR, Schnabel RB. Computational experience with confidence region and confidence interval for nonlinear least squares. *Technometrics*. 1987;29:67.
38. Kulkarni K, Zhang L, Linninger AA. Model and parameter uncertainty in distributed systems. *Ind Eng Chem Res*. 2006;45:7832.
39. Bard Y. *Nonlinear parameter estimation*. New York: Academic Press; 1974.
40. Fogler HS. *Elements of chemical reaction engineering*. 3rd ed. New Jersey: Prentice-Hall Inc. 1999.
41. Pita J, Balakotaiah V, Luss D. Thermoflow multiplicity in a packed-bed reactor: condition and cooling effects. *AIChE J*. 1989; 35:373.
42. Villadsen JV, Michelsen ML. *Solution of differential equations by polynomial approximation*. New York: Prentice-Hall; 1978.
43. Zhang L, Linninger AA. Towards computer-aided separation synthesis. *AIChE J*. 2006;52:1392.
44. More JJ, Sorenson DC, Garbow BS, Hillstrom KE. The MINPACK project. In: Wayne RC. *Sources and Development of Mathematical Software*. 1984:88.

45. Itle GC, Salinger AG, Pawlowski RP, Shadid JN, Biegler LT. A tailored optimization strategy for PDE-based design: application to a CVD reactor. *Comput Chem Eng*. 2004;28:291.
46. Schmid C, Biegler LT. Quadratic programming algorithms for reduced hessian SQP. *Comp Chem Eng*. 1994;18:817.
47. Kunisch K, Sachs EW. Reduced SQP methods for parameter identification problems. *SIAM J Numerical Analysis*. 1992;29:1793–1820.
48. Guay M, Mclean DD. Optimization and sensitivity analysis for multireponse parameter estimation in systems of ordinary differential equations. *Comput Chem Eng*. 1995;19:1271.
49. Lucia A, Fang Y. Multivariable terrain methods. *AIChE J*. 2003;49: 2553.
50. Papamichail I, Adjiman CS. Global optimization of dynamic systems. *Comput Chem Eng*. 2004;28:403.
51. Esposito WR, Floudas CA, Global optimization for the parameter estimation of differential-algebraic systems. *Ind Eng Chem Res*. 2000; 39:1291.
52. Esposito WR, Floudas CA. Parameter estimation in nonlinear algebraic models via global optimization. *Comput Chem Eng*. 2002;22: 213
53. Kawajiri Y, Biegler LT. Optimization strategies for simulated moving bed and powerfeed processes. *AIChE J*. 2006;52:1343.
54. Kearfott RB. *Rigorous global search: Continuous problems*. Dordrecht, Netherlands: Kluwer Academic Publishers; 1996.
55. Sahinidis V. BARON: A general purpose global optimization software package. *J Glob Optim*. 1996;8:201.

Appendix A: Derivation of Transport Equations in Curvilinear Coordinates

Metrics of transformation. It is assumed that there is a unique, single valued relationship between the generalized and the physical coordinates as shown in Figure 1, which can be written as:

$$\xi = \xi(x, y),\ \eta = \eta(x, y) \tag{A1}$$

and there exists also the inverse relationship.

$$x = x(\xi, \eta),\ y = y(\xi, \eta) \tag{A2}$$

Important transport terms can be expressed in different reference frames, that is, first derivatives with respect to x, y become:

$$\begin{aligned}\frac{\partial}{\partial x} &= \frac{y_\eta}{|\jmath^{-1}|}\frac{\partial}{\partial \xi} - \frac{y_\xi}{|\jmath^{-1}|}\frac{\partial}{\partial \eta}\\ \frac{\partial}{\partial y} &= \frac{-x_\eta}{|\jmath^{-1}|}\frac{\partial}{\partial \xi} + \frac{x_\xi}{|\jmath^{-1}|}\frac{\partial}{\partial \eta}\end{aligned} \tag{A3}$$

where $|\jmath^{-1}|$ is the determinant of the inverse Jacobian, given by $|\jmath^{-1}| = x_\xi y_\eta - x_\eta y_\xi$.

Curvilinear coordinate transformation for convection–diffusion species transport;

Equation 2 becomes with the help of Eq. A3.

$$\rho\frac{\partial(U\phi)}{\partial\xi} + \rho\frac{\partial(V\phi)}{\partial\eta} - \left[\frac{\partial}{\partial\xi}\left(\Gamma\left[\frac{q_1}{|\jmath^{-1}|}\frac{\partial\phi}{\partial\xi} - \frac{q_2}{|\jmath^{-1}|}\frac{\partial\phi}{\partial\eta}\right]\right) + \frac{\partial}{\partial\eta}\left(\Gamma\left[\frac{q_3}{|\jmath^{-1}|}\frac{\partial\phi}{\partial\eta} - \frac{q_2}{|\jmath^{-1}|}\frac{\partial\phi}{\partial\xi}\right]\right)\right] - |\jmath^{-1}|S = 0 \tag{A4}$$

where $U = (uy_\eta - vx_\eta)$ and $V = (-uy_\xi + vx_\xi)$, and

$$\begin{aligned}q_1 &= x_\eta^2 + y_\eta^2\\ q_2 &= x_\xi x_\eta + y_\xi y_\eta\\ q_3 &= x_\xi^2 + y_\xi^2\end{aligned} \tag{A5}$$

The general formulation, Eq. A4, can be expressed for continuity, momentum, species and energy equations as:

ϕ	Γ	S	Transport equation in curvilinear coordinates		
1	0	0	$\rho\frac{\partial(U\phi)}{\partial\xi} + \rho\frac{\partial(V\phi)}{\partial\eta} = 0$	Continuity	(A6)
u	μ	$-\nabla_x p$	$\rho\frac{\partial(Uu)}{\partial\xi} + \rho\frac{\partial(Vu)}{\partial\eta} + \left(y_\eta\frac{\partial p}{\partial\xi} - y_\xi\frac{\partial p}{\partial\eta}\right) - \left[\frac{\partial}{\partial\xi}\left(\mu\left[\frac{q_1}{\lvert\jmath^{-1}\rvert}\frac{\partial u}{\partial\xi} - \frac{q_2}{\lvert\jmath^{-1}\rvert}\frac{\partial u}{\partial\eta}\right]\right) + \frac{\partial}{\partial\eta}\left(\mu\left[\frac{q_3}{\lvert\jmath^{-1}\rvert}\frac{\partial u}{\partial\eta} - \frac{q_2}{\lvert\jmath^{-1}\rvert}\frac{\partial u}{\partial\xi}\right]\right)\right] = 0$	u-momentum equation	(A7)
v	μ	$-\nabla_y p$	$\rho\frac{\partial(Uv)}{\partial\xi} + \rho\frac{\partial(Vv)}{\partial\eta} + \left(-x_\eta\frac{\partial p}{\partial\xi} + x_\xi\frac{\partial p}{\partial\eta}\right) - \left[\frac{\partial}{\partial\xi}\left(\mu\left[\frac{q_1}{\lvert\jmath^{-1}\rvert}\frac{\partial v}{\partial\xi} - \frac{q_2}{\lvert\jmath^{-1}\rvert}\frac{\partial v}{\partial\eta}\right]\right) + \frac{\partial}{\partial\eta}\left(\mu\left[\frac{q_3}{\lvert\jmath^{-1}\rvert}\frac{\partial v}{\partial\eta} - \frac{q_2}{\lvert\jmath^{-1}\rvert}\frac{\partial v}{\partial\xi}\right]\right)\right] = 0$	v-momentum equation	(A8)
C	D	$r = kc^r$	$\rho\frac{\partial(UC)}{\partial\xi} + \rho\frac{\partial(VC)}{\partial\eta} - \left[\frac{\partial}{\partial\xi}\left(D\left[\frac{q_1}{\lvert\jmath^{-1}\rvert}\frac{\partial C}{\partial\xi} - \frac{q_2}{\lvert\jmath^{-1}\rvert}\frac{\partial C}{\partial\eta}\right]\right) + \frac{\partial}{\partial\eta}\left(D\left[\frac{q_3}{\lvert\jmath^{-1}\rvert}\frac{\partial C}{\partial\eta} - \frac{q_2}{\lvert\jmath^{-1}\rvert}\frac{\partial C}{\partial\xi}\right]\right)\right] - \lvert\jmath^{-1}\rvert r = 0$	Species equation	(A9)
T	k	Q	$\frac{\partial(UT)}{\partial\xi} + \frac{\partial(VT)}{\partial\eta} - \left[\frac{\partial}{\partial\xi}\left(k\left[\frac{q_1}{\lvert\jmath^{-1}\rvert}\frac{\partial T}{\partial\xi} - \frac{q_2}{\lvert\jmath^{-1}\rvert}\frac{\partial T}{\partial\eta}\right]\right) + \frac{\partial}{\partial\eta}\left(k\left[\frac{q_3}{\lvert\jmath^{-1}\rvert}\frac{\partial T}{\partial\eta} - \frac{q_2}{\lvert\jmath^{-1}\rvert}\frac{\partial T}{\partial\xi}\right]\right)\right] - \lvert\jmath^{-1}\rvert Q = 0$	Energy equation	(A10)

Table B1. Discretization Coefficients with Upwinding in Generalized Curvilinear Co-ordinates

$$a_E = \Gamma \frac{q_1}{|J^{-1}|}\bigg|_e + \max(-\rho U|_e, 0),$$
$$a_W = \Gamma \frac{q_1}{|J^{-1}|}\bigg|_w + \max(\rho U|_w, 0), \quad \text{(B1)}$$

$$a_N = \Gamma \frac{q_3}{|J^{-1}|}\bigg|_n + \max(-\rho V|_n, 0),$$
$$a_S = \Gamma \frac{q_3}{|J^{-1}|}\bigg|_s + \max(\rho V|_s, 0), \quad \text{(B2)}$$

$$a_p = a_E + a_W + a_N + a_S,$$

$$H_T = -\Gamma \frac{q_2}{|J^{-1}|}\frac{\partial \phi}{\partial \eta}\bigg|_e + \Gamma \frac{q_2}{|J^{-1}|}\frac{\partial \phi}{\partial \eta}\bigg|_w - \Gamma \frac{q_2}{|J^{-1}|}\frac{\partial \phi}{\partial \xi}\bigg|_n + \Gamma \frac{q_2}{|J^{-1}|}\frac{\partial \phi}{\partial \xi}\bigg|_s \quad \text{(B3)}$$

Appendix B

The transport coefficients for the governing equations in generalized curvilinear coordinates are given in Table B1. When $q_2 = 0$ in orthogonal grids, the source term, H_r becomes 0. The indices, *N, E, S, W,* refer to the cells adjacent to the control balance envelope, *P* (see Figure B1).

Appendix C

Discretized form of generalized equations for each case study

Discovery of Cerebral Transport and Metabolic Reaction Properties. This section provides more details on the problem equations for each case study. The equations for the Fdopa and Methyl-Fdopa clearance are shown in Cartesian form below:

$$\frac{\partial}{\partial x}\left(D_D \frac{\partial C_D}{\partial x}\right) + \frac{\partial}{\partial y}\left(D_D \frac{\partial C_D}{\partial y}\right) = K_1 C_a - k_2 C_D \quad \text{(C1)}$$

$$\frac{\partial}{\partial x}\left(D_M \frac{\partial C_M}{\partial x}\right) + \frac{\partial}{\partial y}\left(D_M \frac{\partial C_M}{\partial y}\right) = \kappa K_1 C_m - \kappa k_2 C_M \quad \text{(C2)}$$

Using the generalized curvilinear coordinates transformation as shown in Appendix A the Eqs. C1 and C2 are transformed to Eqs. C3 and C4:

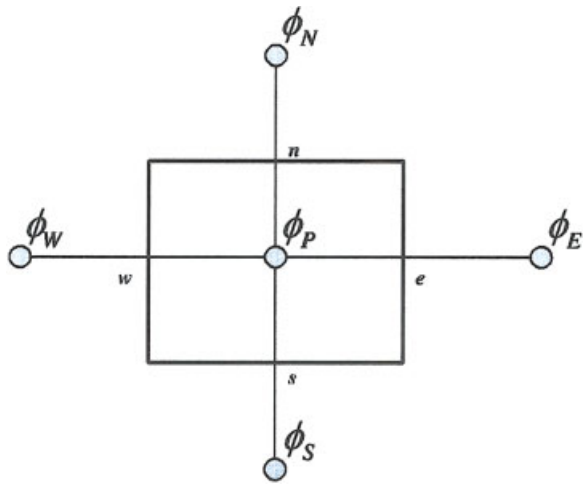

Figure B1. Control balance envelope of a finite volume for a scalar transport quantity ϕ (*T, C*, etc.).

The capital indices *N*, *E*, *S*, *W*, refer to cells adjacent to the control envelop. The small indices *n*, *e*, *s*, *w*, refer to the faces of the control envelop. [Color figure can be viewed in the online issue, which is available at www. interscience. wiley.com.]

$$\frac{\partial}{\partial \xi}\left(D_D\left[\frac{q_1}{|\jmath^{-1}|}\frac{\partial C_D}{\partial \xi} - \frac{q_2}{|\jmath^{-1}|}\frac{\partial C_D}{\partial \eta}\right]\right) + \frac{\partial}{\partial \eta}\left(D_D\left[\frac{q_3}{|\jmath^{-1}|}\frac{\partial C_D}{\partial \eta} - \frac{q_2}{|\jmath^{-1}|}\frac{\partial C_D}{\partial \xi}\right]\right) = |\jmath^{-1}|K_1 C_a - |\jmath^{-1}|k_2 C_D \quad \text{(C3)}$$

$$\frac{\partial}{\partial \xi}\left(D_M\left[\frac{q_1}{|\jmath^{-1}|}\frac{\partial C_M}{\partial \xi} - \frac{q_2}{|\jmath^{-1}|}\frac{\partial C_M}{\partial \eta}\right]\right) + \frac{\partial}{\partial \eta}\left(D_M\left[\frac{q_3}{|\jmath^{-1}|}\frac{\partial C_M}{\partial \eta} - \frac{q_2}{|\jmath^{-1}|}\frac{\partial C_M}{\partial \xi}\right]\right) = |\jmath^{-1}|\kappa K_1 C_m - |\jmath^{-1}|\kappa k_2 C_M \quad \text{(C4)}$$

The finite volume discretization of C3 and C4 gives C5–C7 for the Fdopa clearance, and C8–C10 for the Methyl-Fdopa clearance

$$a_P C_{D_P} - a_E C_{D_E} - a_W C_{D_W} - a_N C_{D_N} - a_S C_{D_S} - H_D = 0 \quad \text{(C5)}$$

$$a_E = D_D \frac{q_1}{|\jmath^{-1}|}\bigg|_e,\ a_W = D_D \frac{q_1}{|\jmath^{-1}|}\bigg|_w,$$
$$a_N = D_D \frac{q_3}{|\jmath^{-1}|}\bigg|_n,\ a_S = D_D \frac{q_3}{|\jmath^{-1}|}\bigg|_s,$$
$$a_P = a_E + a_W + a_N + a_S, \quad \text{(C6)}$$

$$H_D = -D_D \frac{q_2}{|\jmath^{-1}|}\frac{\partial C_D}{\partial \eta}\bigg|_e + D_D \frac{q_2}{|\jmath^{-1}|}\frac{\partial C_D}{\partial \eta}\bigg|_w - D_D \frac{q_2}{|\jmath^{-1}|}\frac{\partial C_D}{\partial \xi}\bigg|_n + D_D \frac{q_2}{|\jmath^{-1}|}\frac{\partial C_D}{\partial \xi}\bigg|_s + |\jmath^{-1}|K_1 C_a - |\jmath^{-1}|k_2 C_D \quad \text{(C7)}$$

Table C1. Boundary Conditions and Grid Size of Discretized Domains for the Three Case Studies

	L-Dopa	Plutonium Tank	Catalytic Pellet Reactor
Number of Finite Volumes	179	$12 \times 10 = 120$	$10 \times 20 = 200$
Boundary conditions	Impermeable surfaces $\frac{dC}{dn} = 0$	On curved surface, top and bottom surfaces $(\alpha \frac{dT}{dn})_s = h_{ext}\,[T_a - T\|_s]$	Inlet: C = 1.6E-6 mol/cm^3
		Zero flux in the center $\frac{dT}{dr} = 0$	T = 298.1 K
			Outlet: full developed flow; $\frac{dC}{dz} = 0$, $\frac{dT}{dz} = 0$
			On curved surface: $\frac{dC}{dr} = 0$; $(k_e \frac{dT}{dr})_R = h[T_a - T\|_R]$
Geometry	Unstructured grid	Two-dimensional structured grid cylinder	Two-dimensional structured grid cylinder
Number of state variables	526	168	1300
Number of sensitivity variables	2104	404	3900

$$b_P C_{M_P} - b_E C_{M_E} - b_W C_{M_W} - b_N C_{M_N} - b_S C_{M_S} - H_M = 0 \tag{C8}$$

$$b_E = D_M \frac{q_1}{|\jmath^{-1}|}\bigg|_e,\ b_W = D_M \frac{q_1}{|\jmath^{-1}|}\bigg|_w,$$
$$b_N = D_M \frac{q_3}{|\jmath^{-1}|}\bigg|_n,\ b_S = D_M \frac{q_3}{|\jmath^{-1}|}\bigg|_s,$$
$$b_P = b_E + b_W + b_N + b_S, \tag{C9}$$

$$\mathrm{H}_M = -D_M \frac{q_2}{|\jmath^{-1}|}\frac{\partial C_M}{\partial \eta}\bigg|_e + D_M \frac{q_2}{|\jmath^{-1}|}\frac{\partial C_M}{\partial \eta}\bigg|_W - D_M \frac{q_2}{|\jmath^{-1}|}\frac{\partial C_M}{\partial \xi}\bigg|_n + D_M \frac{q_2}{|\jmath^{-1}|}\frac{\partial C_M}{\partial \xi}\bigg|_s + |\jmath^{-1}|\kappa K_1 C_m - |\jmath^{-1}|\kappa k_2 C_M \tag{C10}$$

Plutonium Oxide Storage Tank. The heat conduction problem of Eq. 16 can be written in cylindrical coordinated as in C11.

$$\frac{\partial}{\partial r}\left(r\alpha\frac{\partial T}{\partial r}\right) + r\frac{\partial}{\partial z}\left(\alpha\frac{\partial T}{\partial z}\right) + qr = 0;\ \alpha = k_1 + k_2 T^3 \tag{C11}$$

Integrating C11 over one control volume delineated by faces *n, e, s, w* gives:

$$\int_s^n \int_w^e \left[\frac{\partial}{\partial r}\left(r\alpha\frac{\partial T}{\partial r}\right) + r\frac{\partial}{\partial z}\left(\alpha\frac{\partial T}{\partial z}\right)\right] drdz = \int_s^n \int_w^e [-qr] drdz;\ \alpha = k_1 + k_2 T^3 \tag{C12}$$

Solving the volume integral using proper profile assumptions yield:

$$\left[\left(r\alpha\frac{\partial T}{\partial r}\right)_e - \left(r\alpha\frac{\partial T}{\partial r}\right)_w\right][z_n - z_s] + \frac{1}{2}\left[r_e^2 - r_w^2\right] \times \left[\left(\alpha\frac{\partial T}{\partial r}\right)_n - \left(\alpha\frac{\partial T}{\partial r}\right)_s\right] = \frac{-q}{2}\left[r_e^2 - r_w^2\right][z_n - z_s] \tag{C13}$$

where, α is the effective thermal conductivity. Thus, the discretization of the Plutonium oxide storage tank leads to an algebraic equation for each volume.

$$a_P T_P - a_E T_E - a_W T_W - a_N T_N - a_S T_S - q\Delta V = 0 \tag{C14}$$

the coefficients are given below

$$a_E = \frac{1}{\Delta r}\left(r_P + \frac{1}{2}\Delta r\right)\left(k_1 + \frac{k_2}{8}(T_P + T_E)^3\right),$$
$$a_W = \frac{1}{\Delta r}\left(r_P - \frac{1}{2}\Delta r\right)\left(k_1 + \frac{k_2}{8}(T_P + T_W)^3\right) \tag{C15}$$
$$a_N = r_P\left(\frac{\Delta r}{\Delta z}\right)\left(k_1 + \frac{k_2}{8}(T_P + T_N)^3\right),$$
$$a_W = r_P\left(\frac{\Delta r}{\Delta z}\right)\left(k_1 + \frac{k_2}{8}(T_P + T_S)^3\right) \tag{C16}$$
$$a_P = a_E + a_W + a_N + a_S,\ \Delta V = r\Delta r\Delta z$$

Catalytic Pellet Reactor. Since the storage vessel is cylindrical, the curvilinear transformation relationship can be obtained analytically, according to the following balances $|\jmath^{-1}| = r$, $x_\xi = \cos\omega$, $x_\zeta = 0$, $y_\xi = \sin\omega$, $y_\eta = r\cos\omega$, $y_\zeta = 0$, $z_\zeta = 0$, $z_\eta = 0$, $z_\zeta = 1$. Accordingly, the vectorial form of species and energy transport in the pellet, Eqs. 22 and 23, can be expressed as in C17 and C18.

$$u\frac{dC_A}{dz} + v\frac{dC_A}{dr} = D_{AB}\frac{d^2C_A}{dz^2} + D_{AB}\frac{1}{r}\frac{d}{dr}\left(r\frac{dC_A}{dr}\right) + r_A\rho_b \tag{C17}$$

$$\rho_g C_p u\frac{dT}{dr} + \rho_g C_p v\frac{dT}{dz} = k_e\frac{d^2T}{dz^2} + k_e\frac{1}{r}\frac{d}{dr}\left(r\frac{dT}{dr}\right) + r_A\Delta H \tag{C18}$$

Integration of conservation balances for each transport quantity, C_A and T, along the *r*- and *z*-directions over each volume gives the following results.

$$\int_w^e\int_s^t\left(u\frac{dC_A}{dz} + v\frac{dC_A}{dr} - D_{AB}\frac{d^2C_A}{dz^2} - D_{AB}\frac{1}{r}\frac{d}{dr}\left(r\frac{dC_A}{dr}\right) - r_A\rho_b\right) drdz = 0 \tag{C19}$$

$$\int_w^e\int_s^t\left(\rho_g C_p u\frac{dT}{dr} + \rho_g C_p v\frac{dT}{dz} - k_e\frac{d^2T}{dz^2} - k_e\frac{1}{r}\frac{d}{dr}\left(r\frac{dT}{dr}\right) - r_A\Delta H\right) drdz = 0 \tag{C20}$$

$$uC_A r\Delta r|_e - uC_A r\Delta r|_w + vC_A r\Delta z|_n - vC_A r\Delta z|_s - \left(D_{AB}\frac{dC_A}{dz} r\Delta r|_e - D_{AB}\frac{dC_A}{dz} r\Delta r|_w\right) - \left(D_{AB} r\frac{dC_A}{dr}\Delta z|_n - D_{AB} r\frac{dC_A}{dr}\Delta z|_s\right) - r_A\rho_b r\Delta r\Delta z = 0 \quad \text{(C21)}$$

$$uC|_e r\Delta r - uC|_w r\Delta r + vC|_n r\Delta z - vC|_s r\Delta z - \left(D_{AB} r\Big|_e \frac{C_E - C_P}{\delta z}\Delta r - D_{AB} r\Big|_w \frac{C_P - C_W}{\delta z}\Delta r\right) - \left(D_{AB} r\Big|_n \frac{C_N - C_P}{\delta r}\Delta z - D_{AB} r\Big|_s \frac{C_P - C_S}{\delta r}\Delta z\right) - r_A\rho_b r\Delta r\Delta z = 0 \quad \text{(C22)}$$

Using the convention of Figure B1 and upwinding, the discretized equation of species transport can be written as in (C23).

$$a_P C_P - a_E C_E - a_W C_W - a_N C_N - a_S C_S - r_A\rho_A \cdot \Delta V = 0 \quad \text{(C23)}$$

with coefficients

$$a_E = \frac{D_{AB} r|_e \Delta r}{\delta z|_e} + \max(-u|_e r\Delta r, 0),$$
$$a_W = \frac{D_{AB} r|_w \Delta r}{\delta z|_w} + \max(u|_w r\Delta r, 0) \quad \text{(C24)}$$

$$a_N = \frac{D_{AB} r|_n \Delta z}{\delta r|_n} + \max(-v|_n r\Delta z, 0),$$
$$a_S = \frac{D_{AB} r|_s \Delta z}{\delta r|_s} + \max(v|_s r\Delta z, 0) \quad \text{(C25)}$$
$$a_P = a_E + a_W + a_N + a_S, \Delta V = r\Delta r\Delta Z$$

The discretized heat-transfer equation in each volume becomes:

$$a_P T_P - a_E T_E - a_W T_W - a_N T_N - a_S T_S - r_A\Delta H \cdot \Delta V = 0 \quad \text{(C26)}$$

where

$$a_E = \frac{k_e r|_e \Delta r}{\delta z|_e} + \max(-\rho C_p u|_e r\Delta r, 0),$$
$$a_W = \frac{k_e r|_w \Delta r}{\delta z|_w} + \max(\rho C_p u|_w r\Delta r, 0) \quad \text{(C27)}$$

$$a_N = \frac{k_e r|_n \Delta z}{\delta r|_n} + \max(-\rho C_p v|_n r\Delta z, 0),$$
$$a_S = \frac{k r|_s \Delta z}{\delta r|_s} + \max(\rho C_p v|_s r\Delta z, 0) \quad \text{(C28)}$$
$$a_P = a_E + a_W + a_N + a_S, \Delta V = r\Delta r\Delta z$$

Boundary conditions and grid size of discretized domains for the three case studies are given in Table C1.

Manuscript received Apr. 28, 2006, and revision received Aug. 23, 2006.